Supporting Information

Sridharan *et al.* 10.1073/pnas.0800005105

SI Text

Materials and Methods. ***fMRI acquisition.*** Brain images were acquired on a 3T GE Signa scanner using a standard GE whole head coil (software Lx 8.3). For the first (auditory event segmentation) experiment, images were acquired every 2 sec in two runs that lasted 9 min 42 sec and 8 min 48 sec, respectively (for a total of 18 min and 30 sec). The second (visual oddball) and third (resting state) scans were acquired in a single run of 7 min 48 sec and 8 min, respectively. A custom-built head holder was used to prevent head movement. Twenty-eight axial slices (4.0-mm thick, 0.5-mm skip) parallel to the AC-PC line and covering the whole brain were imaged using a T2* weighted gradient echo spiral pulse sequence (TR = 2,000 msec, TE = 30 msec, flip angle = 70 deg, and 1 interleave, in-plane spatial resolution of 3.125 mm) (1). To reduce blurring and signal loss arising from field inhomogeneities, an automated high-order shimming method based on spiral acquisitions was used before acquiring functional MRI scans (2). Images were reconstructed by gridding interpolation and inverse Fourier transform for each time point into $64 \times 64 \times 28$ image matrices (voxel size $3.125 \times 3.125 \times 4.5$ mm). A linear shim correction was applied separately for each slice during reconstruction using a magnetic field map acquired automatically by the pulse sequence at the beginning of the scan (1). fMRI data acquisition was synchronized to stimulus presentation using a TTL pulse sent by EPRIME to the scanner timing board.

fMRI data analysis. fMRI data were preprocessed using SPM2 (http://www.fil.ion.ucl.ac.uk/spm). Functional volumes were corrected for movement-related effects (3), spatially normalized to stereotaxic Talairach coordinates, resampled every 2 mm using sinc interpolation, and smoothed with a 4-mm Gaussian kernel to reduce spatial noise. For the first (auditory segmentation) and second (visual oddball) experiments, statistical analysis was performed using the general linear model (GLM) and the theory of Gaussian random fields as implemented in SPM2. A within-subjects procedure was used to model all of the effects of interest for each subject. Confounding effects of fluctuations in global mean were removed by proportional scaling where, for each time point, each voxel was scaled by the global mean at that time point (4). Low-frequency noise was removed with a high-pass filter (0.5 cycles/min) applied to the fMRI time series at each voxel. Effects of interest for each subject were then defined with the relevant contrasts of the parameter estimates. Group analysis was performed using a random-effects model that incorporated a two-stage hierarchical procedure. In the first stage, contrast images for each subject and each effect of interest were generated as described above. In the second stage, these contrast images were analyzed using a general linear model to determine voxel-wise t statistics. Finally, the t statistics were normalized to Z scores, and significant clusters of activation were determined using the joint expected probability distribution of height and extent of Z scores (5), with height ($Z > 2.33$; $P < 0.01$) and extent thresholds ($P < 0.05$). Maxima and all coordinates are reported in MNI coordinates. Activations were overlaid on a structural Talairach template image using MRIcro (http://www.sph.sc.edu/comd/rorden/mricro.html).

Independent component analysis. Data from the first session of the scan were preprocessed with SPM2 as described above. The preprocessed data were then downsampled to one-half its original resolution (by sampling alternate points) in each dimension to reduce the heavy memory requirements imposed by ICA. ICA was then performed on the preprocessed, downsampled data using the Melodic software package (http://www.fmrib.ox.ac.uk/fsl/). Similar independent components were grouped across subjects using an in-house clustering algorithm; the algorithm computes a similarity metric using the inter-subject correlations of both the spatial map and the associated time course to create groups of similar components across subjects (6). Components in a cluster were then masked with a gray-matter mask and entered into a second random effects analysis (6) and height thresholded at the $P < 0.001$ level, uncorrected, to create group independent component maps.

Calculation of* peak latency *differences. We used the method developed by Henson and colleagues (7) to identify brain regions where the peak of the BOLD response occurred earlier/later relative to the transition. Briefly, this method uses a first-order Taylor approximation (including temporal derivative) in modeling the canonical hemodynamic response function; the ratio of the derivative to canonical parameter estimates provides a measure of the latency differences at each voxel, from which statistical parametric maps may be constructed for each subject. A group map of BOLD latency was then created by entering the individual subject latency images (smoothed with an 8-mm FWHM isotropic Gaussian kernel) into a second-level random-effects analysis. Group-level latency SPMs were masked with voxels that survived the $P < 0.05$ (corrected) level in the F tests in the original SPMs. The group map was height thresholded at $P < 0.025$ uncorrected, and only regions comprising at least ten contiguous voxels are reported.

Calculation of* onset latency *differences. Differences in peak latency of the BOLD response between regions may arise from differences in either the onset or the duration of neural activity (7). Onset latency of the BOLD response provides a means, in principle, of decoupling these possibilities so as to uncover the underlying pattern of neural activity onsets (7–10). We calculated onset latencies according to the method developed by Sterzer and Kleinschmidt (8). This method uses a Fourier model that fits the BOLD response as a linear combination of Fourier basis functions; this removes the need for assuming a response shape *a priori*. The mean time-series extracted from each ROI for each subject was fitted with a sixth-order Fourier basis set (windowed with a Hanning function). Onset latencies were defined as the time at which the slope of the fitted response exceeded 10% of the maximum slope of the ascending part of the response. We then performed a two-sample *t*-test to identify brain regions significantly differing in the onsets of their neural activity ($q < 0.05$, FDR corrected for multiple comparisons).

Granger causality analysis (GCA). GCA was performed in accordance with the methods of Roebroeck *et al.* (11). First, the mean time course from each ROI was extracted for all subjects. This time course was then high-pass filtered at 0.5 cycles per minute. GCA was performed to test for causal influences between ROIs taken pairwise. The order of the autoregressive model used for computation of the influence measure was selected using the Bayesian information criterion. We report the raw values of the directed influence terms for the three tasks in Table S4 *A.1*, *B.1*, and *C.1*. We proceeded to construct a causal connectivity graph (Fig. 3, main text) from these raw F-values as described next.

We performed statistical inference on the causal connections using bootstrap analysis: block-randomized time courses were used to generate an empirical null distribution of influence terms (F-values) and their differences (11) (the difference terms may be obtained by subtracting terms symmetrically situated about the main diagonal in Table S4 *A.1*, *B.1*, and *C.1*). Those directed

connections whose median (across subjects) was significantly different from the median of the null (F-value) distribution (gray arrows in Fig. 3, main text) were identified using a Mann-Whitney *U* test and a stringent threshold ($P < 0.01$, Bonferroni corrected for multiple comparisons). The stringent threshold (and correction) were chosen to avoid potentially spurious causal links introduced by the low temporal resolution and hemodynamic blurring in the fMRI signal. In addition, a difference of influence term ($F_{x\rightarrow y}$ - $F_{y\rightarrow x}$) was used to assess links that showed a dominant direction of influence; the difference term further limits potentially spurious links caused by hemodynamic blurring, and permits the use of a less stringent threshold for group-level testing (11). Again, these dominant links were those wherein the median of the difference of influence term significantly differed from the empirically constructed bootstrap (null) distribution (Mann-Whitney *U* test, $P < 0.05$). Red arrows Fig. 3 (main text) and violet boxes in Table S4 (*A.1*, *B.1*, and *C.1*) highlight these dominant directed connections. P-values for these connections are parenthetically mentioned inside the violet boxes in Table S4 (*A.1*, *B.1*, and *C.1*); furthermore, those *P* values that passed the FDR correction for multiple comparisons are highlighted in blue in the table.

To emphasize the complementarity of the causal and instantaneous connectivity, we also report the instantaneous influence term ($F_{x.y}$) which is an indicator of the classic "zero-lag functional connectivity" between each pair of nodes (11) (Table S4 *A.2*, *B.2*, and *C.2*). A separate analysis confirmed that $F_{x.y}$ is an indicator of the "zero-lag" correlation ("r" value) between pairs of regions: $F_{x.y}$ and "r" values are tightly correlated across pairs of ROIs for all tasks ($r \approx 0.9$, $P < 10^{-4}$). The $F_{x.y}$ and ($F_{x\rightarrow y}$ - $F_{y\rightarrow x}$) terms may be used to infer the relative strength of instantaneous vs. causal(directed) interactions, with the caveat that the instantaneous term is likely artificially inflated due to the temporal smoothing introduced by the hemodynamic response (11). Further, to provide concurrent validity to the GCA approach, we attempted to cluster the six ROIs pairwise to maximize the sum of mutual (pairwise) instantaneous influences ($\Sigma F_{x.y}$). Across all experiments, the most optimal clusters (red boxes in Table S4 *A.2*, *B.2*, and *C.2*) were identical with the SN (rFIC, ACC), CEN (rDLPFC, rPPC), and DMN (VMPFC, PPC), further confirming the functional dissociation between these networks that we observed with ICA.

Granger causality and network analyses with two other task paradigms. GCA was performed in two other datasets: (a) A visual "oddball" attention task (12) employing 13 participants, and (b) a resting state scan employing 22 participants. These data were chosen because they involve entirely different stimulus modalities and task requirements. The visual oddball task showed right-lateralized activation of the SN and CEN regions and deactivation of the DMN regions during the perception of the infrequent (as contrasted with frequent) stimuli (data not shown). Similarly, statistical parametric latency maps, as computed by the method of Henson *et al.* (7) revealed that the rFIC and ACC had earlier peak latency compared to other regions in the CEN and DMN (data not shown).

For the visual oddball task, ROIs were defined at each key (SN/CEN/DMN) network region as spheres centered at the peaks of activation (or deactivation) and with radii raging from 6–10 mm. ROIs for the resting state task were the same as those used for the auditory event segmentation task. Time courses were extracted from each ROI, and bivariate GCA was performed as described above for each ROI pair for each task. Network statistics were computed on these causal networks in a manner similar to that described in the main text (see *Materials and Methods*).

Discussion. ***Potential confound: neural vs. vascular effects.*** Information flow between networks of neurons occurs over the timescale of several tens to hundreds of milliseconds, whereas with fMRI we are constrained to imaging the slow variations in the BOLD signal that occurs on the order of a few seconds (albeit with excellent spatial resolution that is impossible to achieve with other scalp-recording techniques that have better temporal resolution, such as electro-encephalograpy or magneto-encephalography). Hence, one potential caveat while performing chronometric and causal analyses on the BOLD signal is that the observed effects may reflect vascular rather than neural dynamics. However, we present several lines of evidence that argue against this possibility:

(*i*) Previous studies have used chronometric techniques, such as onset latency analysis, with carefully controlled experimental designs, to show that the relative timing between onsets of the BOLD responses between different regions can be used as a predictor of differences in neural activity onset, and can resolve these differences with a temporal accuracy of tens to hundreds of milliseconds (8–10)

(*ii*) In a previous analysis of a Sternberg working memory task, wherein a visual stimulus precedes motor response, we have shown, using onset latency chronometric analysis, that the BOLD signal onsets earlier in sensory (visual), compared to motor areas. Similarly, GCA detected a causal influence from the visual to motor areas (13), as expected.

(*iii*) Two recent studies have shown that the BOLD signal is tightly coupled with gamma (30–70 Hz) band-limited-power (BLP) of the intracranial EEG in the visual and auditory cortices (14, 15). Several previous studies have shown that there is increased gamma band activity during visual or tactile attention in primates and humans (16, 17), and during human conscious perception [intracranial EEG recordings, (18)]. Hence, it is plausible that the BOLD signal fluctuations in the CEN and DMN that appear to be caused by the rFIC (Fig. 3, main text) reflect attentional control mechanisms, mediated by gamma power coupling between these regions, that underlie the CEN-DMN switch.

(*iv*) Consistent latency differences and causal effects were observed across three different datasets, each with a large number of subjects, using random effects analyses.

(*v*) The brain regions probed in our study are served by multiple cerebral arteries, so the timing of vascular changes are unlikely to be coupled in any significant way. Moreover, it is plausible to assume that the distribution of vasculature is roughly symmetric across hemispheres: in this case, one would expect that the vascular dynamics in the right hemispheric regions to be mirrored (or closely approximated) by their left hemispheric counterparts. However, in our analysis this was not the case: latency and causal connectivity analysis on the corresponding left hemispheric regions indicated a less robust, and more variable effects, the dynamics were not similar to those of their right hemispheric counterparts (across tasks and subjects); left hemispheric regions often failed to show statistically significant causal and latency effects (Fig. S3).

These lines of evidence increase confidence, and further confirm, that our findings directly reflect the underlying neural processes.

Choice of regions of interest. In the causal connectivity and network analyses outlined in the main text, we have confined ourselves to the six key nodes of the SN, CEN, and DMN, and specifically to the right hemisphere. Since our question of interest was the mechanism of switching between the CEN and DMN, only those regions that showed significant latency differences with the CEN and DMN regions (as assessed by the whole brain peak latency analysis, Fig. S1 and Table S2) were selected for further analysis. In our analysis, only the SN nodes (FIC and ACC) in the prefrontal cortex showed peak latency differences consistently across both auditory segmentation and visual oddball tasks. Hence, we included only the FIC and the ACC (along with the

nodes of the CEN and DMN) for subsequent GCA and network analyses. In this section we briefly discuss control analyses performed with brain regions that could play a role in the switching process, including the left hemispheric counterparts of the FIC, DLPFC, and PPC, the temporoparietal junction (TPJ), a key node implicated in directing bottom-up attention to salient environmental stimuli (19, 20) as well as sensory regions (primary auditory and visual cortex) that could trigger bottom-up signaling

(i) Left hemispheric regions in the SN, CEN, and DMN. Our previous GLM analysis of the auditory event segmentation task data revealed that level of activity in the left hemispheric regions (FIC, DLPFC, and PPC) was significantly lower than that of the corresponding right hemispheric regions [figure 4 in (13)]. GLM analysis of the visual oddball task also indicated significant right lateralization of responses in the regions of interest (12). Hence, we hypothesized that the signals in the left hemispheric regions might be less robust and other effects such as latency, and causality would be correspondingly weaker. There was evidence of this in an analysis of the auditory segmentation task: while the mean onset latencies of the right and left FICs did not differ significantly (two sample t-test, $P > 0.05$), the left FIC onset latencies were highly variable across subjects (0.61 ± 0.62 s, mean $\pm$ SD), compared with the right FIC (0.40 ± 0.18 s). This led to far fewer regions showing significant onset latency differences with the left FIC (only PCC, data not shown), as compared with the right FIC that showed significant latency differences with almost all of the CEN and DMN regions (Fig. 2 in main text). Similarly, the left PPC did not show significant onset latency differences with any region.

To perform connectivity and network analyses on the left hemispheric regions, we defined the following ROIs in the left hemisphere: left-hemispheric FIC (lFIC) and left-hemispheric PPC (lPPC) ROIs were defined as spheres of 6–10-mm radius centered around the peaks of the ICA activation clusters (Table S1); the left-hemispheric DLPFC (lDLPFC) ROI was derived from its right-hemispheric counterpart (Table S1) by reflection about the x = 0 mm sagittal plane. The ACC, VMPFC, and PCC ROIs were identical to ones used in the analysis reported in the main text. Time courses were extracted using Marsbar, and connectivity (GCA) and network analysis were performed as described in the Materials and Methods section in the main text. This analysis revealed that the left FIC did not differ significantly from any of the other regions in its causal outflow (out-in degree) (Fig. S3*A*), or path length (data not shown). Repeating this analysis with the visual oddball and task-free resting state data revealed that the net causal outflow of the left FIC differed from very few regions (Fig. S3 *B* and *C*), whereas the right FIC had a much more robust difference in net causal outflow across all three tasks (compare with Fig. 4, main text).

(ii) Sensory regions vis-à-vis the SN, CEN and DMN. In the present study, the auditory segmentation and visual oddball tasks used different sensory modalities, whereas the resting state task did not require any explicit (task-based) sensory information processing. In fact, analysis of the resting state data also showed that the FIC can exert causal influences across networks without any explicit stimulus. Hence, in the analysis reported in the main text, sensory regions were excluded from connectivity and network analysis to emphasize commonality of directional information flow, and the critical role of the FIC across tasks.

However, examination of the influences of sensory signals on the three networks remains an important open problem. Does the rFIC merely relay bottom-up sensory information from the sensory regions to the other nodes, or truly exert top-down control on the other nodes? To address this question, we performed onset latency and GCA on ROIs in the sensory cortices vis-à-vis the three networks. Briefly, we defined regions of interest as spheres of 6–8-mm radius in the bilateral auditory cortex (Heschl's gyrus, for the auditory segmentation task, MNI coordinates: [$\pm$53, $-$8, 4]mm) and bilateral visual cortex (lingual gyrus, Brodmann Area 18, for the visual oddball task, MNI coordinates: [$\pm$9, $-$82, $-$7]mm). We extracted the time series from these regions as before (see Materials and Methods). It must be noted that, in Experiment 1 (auditory event segmentation), activation in the auditory cortex was positively correlated with amplitude changes in the music; we did not detect any region in the auditory cortex that increased its activity in response to decreased sound amplitude (13). Thus, at the events of interest (musical movement transitions), which are accompanied by a brief silence, we expected auditory cortex activity to be diminished (and this was indeed what we found using a GLM analysis, data not shown). Hence, the time series of the auditory cortices were inverted before further analysis (similar to the VMPFC and PCC, as in Fig. S2), because we hypothesized that the onset of the decrease in activity could, in fact, provide a signal to higher areas and/or prefrontal regions. For Experiment 2 (visual oddball), no such inversion of the signals from the visual cortex was considered necessary.

Latency analysis of the signals from the sensory cortices revealed that the onset latency of these regions did not differ significantly from the rFIC (two-sample t test, $P > 0.05$, Bonferroni correction for multiple comparisons). The auditory and visual cortices demonstrated early onsets (median of 0.3 s to 0.4 s; comparable to the rFIC) although these differences were not statistically significantly different from the other regions (two-sample t test, $P > 0.05$). Similarly, GCA on a network including the sensory regions for the auditory segmentation task revealed a mean $F_{x\to y}$ of 0.0365 from auditory cortex to the rFIC and 0.0323 from the rFIC to the auditory cortex ($P < 0.01$, Mann-Whitney U test, Bonferroni correction for multiple comparisons): the dominant direction of influence (difference term, $F_{x\to y} - F_{y\to x}$) was from the auditory cortex to the rFIC, but this did not reach significance ($P > 0.05$, Mann-Whitney U test). On the other hand, this trend was reversed in the visual oddball task, with a mean $F_{x\to y}$ of 0.0286 from visual cortex to rFIC and 0.0465 from rFIC to visual cortex; again, the dominant direction of influence (in this case from rFIC to visual cortex) did not reach significance. Overall, we found that while there was some evidence of early onset in the sensory cortices across tasks, the directionality of information flow (to and from the rFIC) could not be unambiguously resolved. One possibility here is that there is some sort of early but weak signaling from the sensory regions that is amplified by the FIC. Again, the lack of robust latency differences between the sensory regions and the FIC may be due to the relative insensitivity of fMRI to detect small latency differences. Hence, a proper examination of this issue may require simultaneous EEG and fMRI recordings (12).

(iii) The role of the right temporo-parietal junction (rTPJ) vis-à-vis the right fronto-insular cortex (rFIC) in attention switching. Corbetta & Shulman (19) proposed that the rTPJ is an important component of the bottom-up salience detection system (redirecting endogenous attention to external stimuli). Our data suggest that the rFIC may have primacy in initiating the control signals responsible for switching between endogenous (default-mode) and exogenous attentional systems. In a more recent study, Shulman *et al.* (20) investigated several coordinates in the TPJ region. Of special relevance are two subregions in the right TPJ (rTPJ): one more dorsal (Talairach coordinates: 45, $-$49, 46; or MNI coordinates: 46, $-$52, 47), and the second more ventral (Talairach coordinates: 52, $-$49, 26; or MNI coordinates 53, $-$52, 26). The former region lies in close proximity to the rPPC region that was the focus of our study (MNI coordinates: 54, $-$50, 50). Our analysis indicates that the rFIC had a consistently earlier peak and onset latency compared to the rPPC (Fig. 2, Fig. S1); connectivity and network analyses also demonstrate that the rFIC also has a significantly higher net causal outflow than the rPPC (see Fig. 4,

main text). Intriguingly, the rPPC appeared to relay information from the rFIC to the DMN regions (PCC and VMPFC) in the visual oddball and resting state tasks (Fig. 3 *B* and *C*, main text) indicating that the rPPC may mediate deactivation of the DMN regions based on a control signal from the rFIC.

The latter (more ventral) rTPJ subregion is more proximal to the classic TPJ implicated in detecting changes in the sensory environment (19, 21). We performed control analyses on this region (identified on the basis of GLM activation clusters) for both the auditory segmentation (8-mm sphere centered at [54, −44, 20]mm, MNI) and visual oddball (8-mm sphere centered at [57, −46, 18]mm, MNI) task. These analyses indicated that the rTPJ has an onset that followed the rFIC (mean onset difference 0.25 s for auditory segmentation task, and 0.8 s for the visual oddball task, rFIC leading), but these differences were not statistically significant (two-sample *t*-test, $P > 0.05$). GCA and subsequent network analyses indicated that the dominant causal influence direction in the auditory segmentation task was from the rFIC to the rTPJ with a mean $F_{x\to y}$ of 0.0350 from rFIC to the rTPJ (F:rFIC→rTPJ) and 0.0219 in the reverse direction (F:rTPJ→rFIC) ($P < 0.01$, Mann-Whitney *U* test, Bonferroni correction for multiple comparisons); however, the dominant direction of influence (difference term, $F_{x\to y} - F_{y\to x}$) did not reach significance ($P < 0.05$, Mann-Whitney *U* test). For the visual oddball task these numbers were 0.0620 (F:rFIC→rTPJ) and 0.0474 (F:rTPJ→rFIC), respectively ($P < 0.01$, Mann-Whitney *U* test, Bonferroni correction for multiple comparisons). Moreover, the dominant direction of influence from rFIC to rTPJ was significant at the $P < 0.05$ level (Mann-Whitney *U* test) (Fig. S4). The rFIC also appeared to be more of a central network hub with a higher net causal outflow (1.9 and 1.8 for the two tasks) compared with the rTPJ (0.6 and 0.3 for the two tasks), and shorter path length (1.20 and 1.56 vs. 1.35 and 1.59) although these differences were not statistically significant (two-sample *t*-test, $P > 0.05$) after correcting for multiple comparisons.

In summary, our findings indicate that the rFIC in fact precedes and exerts causal influences on the rTPJ, rather than the other way round, and leads us to hypothesize that the rFIC may, in fact, be the primal circuit breaker that helps redirect endogenous attention in response to salient environmental stimuli.

A brief discussion on Granger Causality Analysis. ***(i) Latency (fMRI mental chronometry) and Granger causality analyses.*** We have used several analyses techniques, viz., peak, onset, and Granger Causality analyses, to examine the dynamics of response in the six key regions of the SN, CEN, and DMN. Here we provide a brief description of how these analyses relate to, and complement each other. The peak latency analysis of (7), provides a statistical parametric map of peak BOLD latencies across the entire brain, which can be used as a starting point for identifying key regions wherein the BOLD response peaks earlier or later, which may be taken as a basic indicator of the relative latency of the underlying neural responses. However, a precise quantification of the latencies in these regions using this approach is not possible due to high estimation errors in the derivative to canonical ratio (7). Moreover, responses of different amplitudes that onset at the same times may peak at different times (with the larger amplitude response having a later peak). To overcome these limitations, we performed onset latency analysis on key regions in the SN, CEN, and DMN [according to the method of Sterzer and Kleinschmidt (8)], which provides a better measure of the relative underlying neural latency differences. Thus, these analyses are complementary, and while one expects early onset regions to also have early peaks (such as we observe in the rFIC), in theory the results from the two analyses need not necessarily overlap.

Again, while peak and onset latency analyses can demonstrate precedence of activation between the CEN-DMN nodes and rFIC, these cannot directly address the presence (or absence) of top-down control that the rFIC would exert on the CEN and DMN regions (22). On the other hand, GCA provides a more principled way to assess top-down control across task paradigms, since it involves contributions from both the stimulus locked BOLD signal as well as stochastic components that are not necessarily stimulus locked (11). In this sense, the two types of analyses are complementary. Findings from onset latency resolved chronometry (fMRI mental chronometry) and GCA need not necessarily overlap, although in practice we do observe significant overlap between these. For instance, the earlier peak and onset latencies of the FIC in the SN are reflective of the underlying causal connectivity pattern with maximal outflow from the FIC across tasks. However, earlier onset alone does not necessarily correspond to a high causal outflow, as evidenced in the ACC, which has a relatively low, and sometimes even negative net causal outflow. These findings are in line with previous observations on these analyses (10, 11, 13, 22).

(ii) Relationship between zero-lag functional connectivity, independent component and Granger causality (causal connectivity) analyses. In our analysis, we have used ICA to show the statistical independence between the SN, CEN, and DMN. ICA performs spatial decomposition to generate maximally independent spatial maps each with an associated timecourse. Each voxel in a spatial ICA map has an identical time-course (except for a scale factor) (23). In this sense, ICA is analogous to functional connectivity in that it identifies spatial clusters of voxels in the brain that have high zero-lag correlations. Moreover, ICA goes beyond traditional functional connectivity analyses by ensuring that noise related components (related to movement, etc.) are factored out of the voxels before the zero-lag spatial correlation maps are computed. There is a fundamental difference between "functional connectivity" as assessed by zero-lag correlation analysis (such as ICA) and "causal connectivity" as assessed by GCA. While ICA decouples these regions (shows them to be functionally disconnected) based on instantaneous correlations, GCA attempts to capture the power of a region's signal to predict the future signal in another region, and evaluates whether these regions are functionally coupled based on the history of the signals (24). For instance, while there is no instantaneous correlation between the different networks, it is possible that these regions are correlated in a time-shifted fashion. While previous studies have shown that the signal in the DMN and CEN/SN are anti-correlated (25, 26), our study replicates this result, and further shows that the BOLD signal in the SN has a shorter onset latency compared to the CEN and the DMN (Fig. 2 and Fig. S2 in our study). GCA exploits this temporal precedence information in a statistical (biviriate/multivariate autoregressive) framework to compute "causal" connectivity between brain regions. However, as a special case, GCA can also be used to capture zero lag correlations using the "instantaneous" term $F_{x.y}$, which approximately corresponds to the residual interactions remaining that could not be assigned a specific directionality (11). Indeed, we found that pairwise clustering of regions based on the instantaneous F term (described previously), revealed that across all experiments, the most optimal clusters (red boxes in Table S4 *A.2*, *B.2*, and *C.2*) were identical with the SN (rFIC, ACC), CEN (rDLPFC, rPPC), and DMN (VMPFC, PPC). Thus, we were able to provide concurrent validity to the GCA approach by confirming the functional dissociation between these networks that we had already observed with ICA (Fig. 1, main text).

1. Glover GH, Lai S (1998) Self-navigated spiral fMRI: Interleaved versus single-shot. *Magn Reson Med* 39:361–368.
2. Kim DH, Adalsteinsson E, Glover GH, Spielman DM (2002) Regularized higher-order in vivo shimming. *Magn Reson Med* 48:715–722.
3. Friston KJ, Williams S, Howard R, Frackowiak RS, Turner R (1996) Movement-related effects in fMRI time-series. *Magn Reson Med* 35:346–355.
4. Macey PM, Macey KE, Kumar R, Harper RM (2004) A method for removal of global effects from fMRI time series. *Neuroimage* 22:360–366.
5. Poline JB, Worsley KJ, Evans AC, Friston KJ (1997) Combining spatial extent and peak intensity to test for activations in functional imaging. *Neuroimage* 5:83–96.
6. Esposito F, *et al.* (2005) Independent component analysis of fMRI group studies by self-organizing clustering. *Neuroimage* 25:193–205.
7. Henson RN, Price CJ, Rugg MD, Turner R, Friston KJ (2002) Detecting latency differences in event-related BOLD responses: Application to words versus nonwords and initial versus repeated face presentations. *Neuroimage* 15:83–97.
8. Sterzer P, Kleinschmidt A (2007) A neural basis for inference in perceptual ambiguity. *Proc Natl Acad Sci USA* 104:323–328.
9. Formisano E, Goebel R (2003) Tracking cognitive processes with functional MRI mental chronometry. *Curr Opin Neurobiol* 13:174–181.
10. Menon RS, Luknowsky DC, Gati JS (1998) Mental chronometry using latency-resolved functional MRI. *Proc Natl Acad Sci USA* 95:10902–10907.
11. Roebroeck A, Formisano E, Goebel R (2005) Mapping directed influence over the brain using granger causality and fMRI. *Neuroimage* 25:230–242.
12. Crottaz-Herbette S, Menon V (2006) Where and when the anterior cingulate cortex modulates attentional response: Combined fMRI and ERP evidence. *J Cogn Neurosci* 18:766–780.
13. Sridharan D, Levitin DJ, Chafe CH, Berger J, Menon V (2007) Neural dynamics of event segmentation in music: Converging evidence for dissociable ventral and dorsal networks. *Neuron* 55:521–532.
14. Privman E, *et al.* (2007) Enhanced category tuning revealed by intracranial electroencephalograms in high-order human visual areas. *J Neurosci* 27:6234–6242.
15. Nir Y, *et al.* (2007) Coupling between neuronal firing rate, gamma LFP, and BOLD fMRI is related to interneuronal correlations. *Curr Biol* 17:1275–1285.
16. Womelsdorf T, Fries P, Mitra PP, Desimone R (2006) Gamma-band synchronization in visual cortex predicts speed of change detection. *Nature* 439:733–736.
17. Bauer M, Oostenveld R, Peeters M, Fries P (2006) Tactile spatial attention enhances gamma-band activity in somatosensory cortex and reduces low-frequency activity in parieto-occipital areas. *J Neurosci* 26:490–501.
18. Meador KJ, Ray PG, Echauz JR, Loring DW, Vachtsevanos GJ (2002) Gamma coherence and conscious perception. *Neurology* 59:847–854.
19. Corbetta M, Shulman GL (2002) Control of goal-directed and stimulus-driven attention in the brain. *Nat Rev Neurosci* 3:201–215.
20. Shulman GL, Astafiev SV, McAvoy MP, d'Avossa G, Corbetta M (2007) Right TPJ deactivation during visual search: Functional significance and support for a filter hypothesis. *Cereb Cortex* 17:2625–2633.
21. Downar J, Crawley AP, Mikulis DJ, Davis KD (2000) A multimodal cortical network for the detection of changes in the sensory environment. *Nat Neurosci* 3:277–283.
22. Goebel R, Roebroeck A, Kim DS, Formisano E (2003) Investigating directed cortical interactions in time-resolved fMRI data using vector autoregressive modeling and granger causality mapping. *Magn Reson Imaging* 21:1251–1261.
23. Beckmann CF, Smith SM (2004) Probabilistic independent component analysis for functional magnetic resonance imaging. *IEEE Trans Med Imaging* 23:137–152.
24. Miller BT, D'Esposito M (2005) Searching for ''the top'' in top-down control. *Neuron* 48:535–538.
25. Greicius MD, Krasnow B, Reiss AL, Menon V (2003) Functional connectivity in the resting brain: A network analysis of the default mode hypothesis. *Proc Natl Acad Sci USA* 100:253–258.
26. Fox MD, Snyder AZ, Zacks JM, Raichle ME (2006) Coherent spontaneous activity accounts for trial-to-trial variability in human evoked brain responses. *Nat Neurosci* 9:23–25.

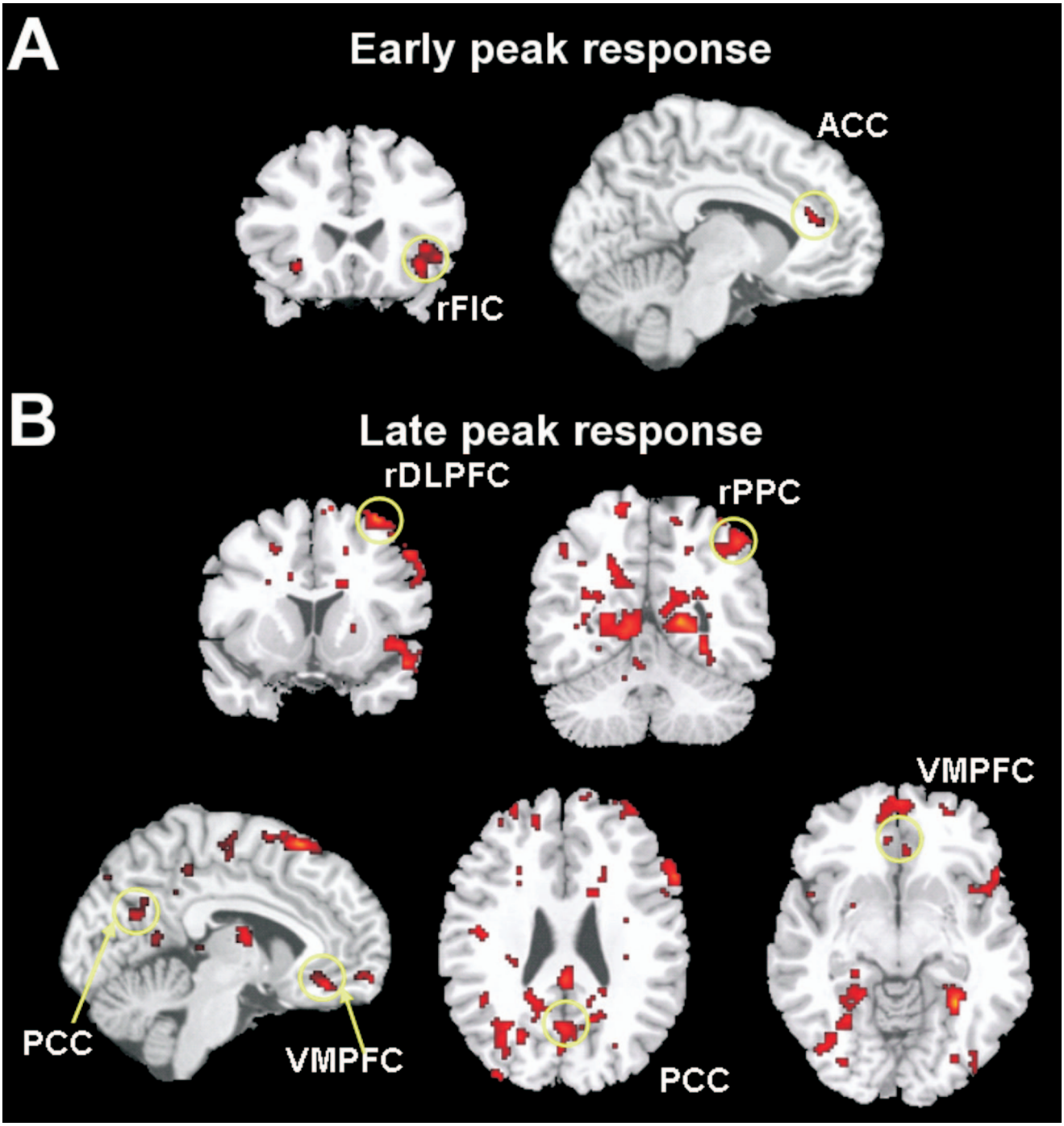

Fig. S1. Differential response latencies at the transition during auditory event segmentation. Latency analysis at the transition revealed early activation in the FIC and ACC, and late activation in the nodes of the CEN and DMN (rDLPFC, rPPC, PCC, and VMPFC). All slices are identical with the slices shown in Fig. 1 of main text, in addition panel (*A*) highlights early response in the ACC in a sagittal slice (see also accompanying Table S2).

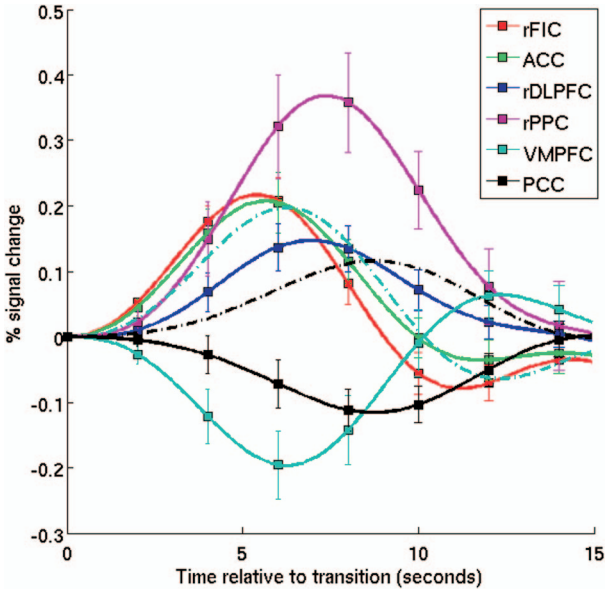

Fig. S2. BOLD response fitted by a Fourier model in the key network regions during auditory event segmentation. The BOLD response was fitted by a sixth-order Fourier model in each of the key nodes of the networks. The fitted responses were averaged across events and subjects for each node and plotted as a percentage signal change from baseline following the occurrence of the event (transition) at t = 0 s. It can be seen that peak activation in the FIC and ACC precedes both peak deactivation in the VMPFC and PCC, and peak activation in the rDLPFC and rPPC. For clarity, the inverted responses in the VMPFC and PCC are shown as dot-dashed lines. Error bars at each TR (2 s) show S.E.M. of the fitted responses across subjects. These fitted responses were further used to define the onset latency for each region (Fig. 2 in main text).

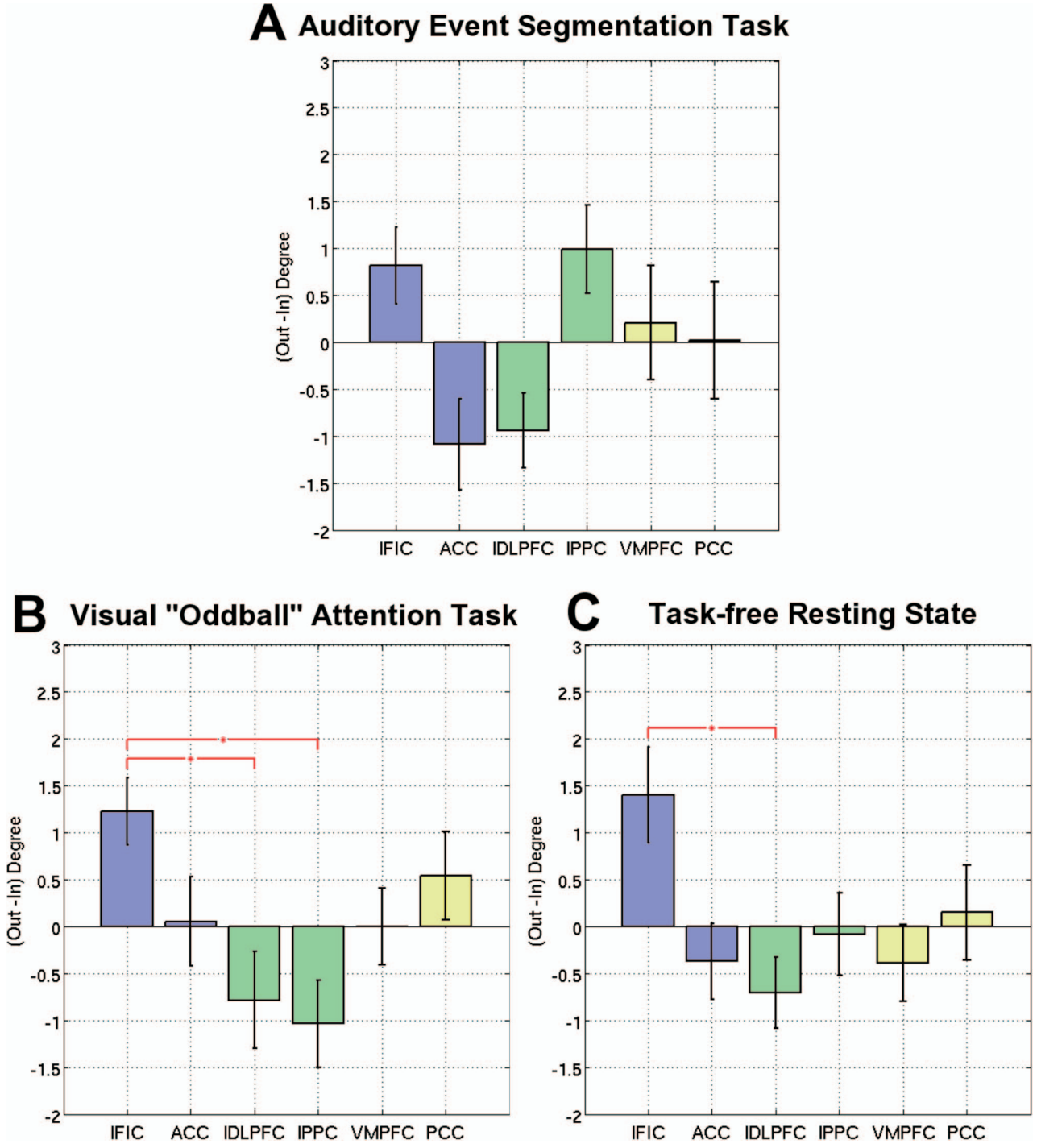

Fig. S3. Net causal outflow (out-in degree) of the left-hemispheric nodes of the Salience, Central-Executive, and Default-Mode Networks in the three experiments. Comparison of the net causal outflow (out-in degree) for the left-hemispheric nodes of the Salience, Central-Executive, and Default-Mode networks (conventions as in Fig. 2, main text). The net causal outflow of the left FIC did not differ significantly from other regions in its causal ''out-in'' degree (a measure of net causal outflow) in a consistent manner across tasks (two-sample test, $q > 0.05$, FDR correction for multiple comparisons), whereas the right FIC had a much more robust difference in net causal outflow across all three tasks (compare with Fig. 4, main text).

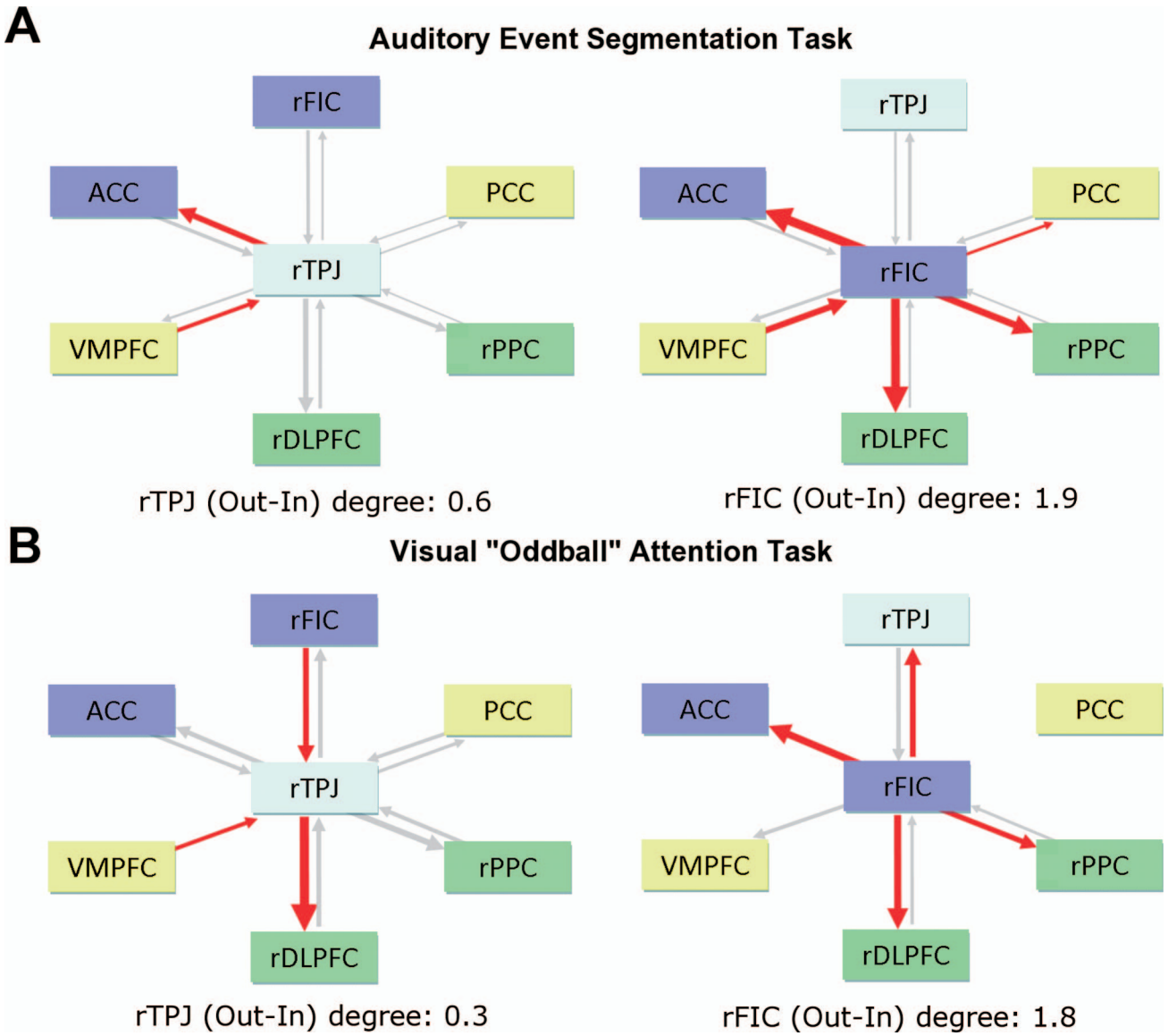

Fig. S4. Granger causality analysis network diagram of the rTPJ and rFIC for the auditory segmentation and visual oddball tasks. Bivariate GCA on the rTPJ (left panel) and rFIC (right panel) with the key nodes of the CEN and DMN in the auditory event segmentation (*A*) and visual oddball (*B*) tasks revealed that the dominant direction of influence was from the rFIC to the rTPJ for both tasks (conventions as in Fig. 3, main text). The rFIC also had a consistently higher net causal outflow (out-in degree, indicated at the bottom of each panel) across both tasks, suggesting that the rFIC may have overall primacy in initiating the switch between exogenous and endogenous attentional systems in the brain [the apparent discrepancy between the net causal outflow values of the rFIC reported here and Fig. 4 (main text), and Table S5, arises from the rTPJ being included here as an additional node in the network analysis].

Table S1. Coordinates of SN, CEN, and DMN regions from ICA-derived clusters of the auditory event segmentation task

Regions	R/L	BA	Peak-MNI cords, mm	Z-Score
Fronto-insular Cortex (FIC)	R	47	37 25 −4	4.98
	L	47	−32 24 −6	4.58
Anterior Cingulate Cortex (ACC)	R/L	24/32	4 30 30	5.80
Dorsolateral Prefrontal Cortex (DLPFC)	R	9	45 16 45	5.14
Posterior Parietal Cortex (PPC)	R	40	54 −50 50	6.18
	L	40	−38 −53 45	4.90
Ventromedial Prefrontal Cortex (VMPFC)	R/L	11	−2 36 −10	4.92
Posterior Cingulate Cortex (PCC)	R/L	23/30	−7–43 33	6.36

Abbreviations: BA, brodmann area; R/L, right or left.

Table S2. Coordinates of SN, CEN, and DMN cluster peaks from peak latency analysis of the auditory event segmentation task (refer to Figure S1)

Regions	R/L	BA	Peak-MNI cords (mm)
Fronto-insular Cortex (FIC)	R	47	34 26 −6
	L	47	−32 25 −10
Anterior Cingulate Cortex (ACC)	R/L	24/32	7 33 19
Dorsolateral Prefrontal Cortex (DLPFC)	R	9	50 15 43
Posterior Parietal Cortex (PPC)	R	40	50 −50 51
	L	40	−46 −50 44
Ventromedial Prefrontal Cortex (VMPFC)	R/L	11	3 37 −14
Posterior Cingulate Cortex (PCC)	R/L	23/30	1 −60 30

Abbreviations: BA, brodmann area; R/L, right or left.

Table S3. Onset latency differences between ROIs during auditory event-segmentation

ROI	rFIC	ACC	rDLPFC	rPPC	VMPFC	PCC
rFIC	N.A.	**0.4958** (*t*=-1.1215, *P*= 0.1163)	**2.0882** (*t*=-3.5800, *P*= 0.0076)	**1.4160** (*t*=-2.3202, *P*= 0.0032)	**1.1345** (*t*=-1.8567, *P*= 0.0031)	**1.7941** (*t*=-2.8595, *P*= 0.0017)
ACC	x	N.A	**1.5924** (*t*=-3.2054, *P*= 0.0528)	**0.9202** (*t*=-2.0128, *P*= 0.0959)	**0.6387** (*t*=-1.5862, *P*= 0.1793)	**1.2983** (*t*=-2.5277, *P*= 0.0391)
rDLPFC	x	x	N.A	**-0.6723** (*t*=-1.0678, *P*= 0.4371)	**-0.9538** (*t*=-0.6990, *P*= 0.2485)	**-0.2941** (*t*=-1.5349, *P*= 0.7454)
rPPC	x	x	x	N.A	**-0.2815** (*t*=-0.8692, *P*= 0.6217)	**0.3782** (*t*=-1.7701, *P*= 0.5839)
VMPFC	x	x	x	x	N.A	**0.6597** (*t*=-1.9409, *P*= 0.3021)
PCC	x	x	x	x	x	N.A

Onset latency differences in seconds (row ROI relative to column ROI). Positive latency differences indicate "row" ROI onsets after "column" ROI (vice versa for negative differences). Significant onset latency differences are highlighted in violet boxes ($P < 0.01$, two-sample *t* test). All highlighted regions also showed significant onset latency differences after FDR correction for multiple comparisons ($q < 0.05$, highlighted in blue, see also Figure 2).

Table S4. Mean GCA directed influence and instantaneous influence F values between pairs of regions for the three experiments

(A) Auditory event segmentation task

(A.1) Directed influence F values (mean ± SE across subjects)

F(x→y)	rFIC	ACC	rDLPFC	rPPC	VMPFC	PCC
rFIC	-	0.031±0.007	0.025±0.007	0.021±0.007	0.064±0.015 (0.0056)	0.028±0.008
ACC	0.092±0.020 (0.0000)	-	0.036±0.009	0.023±0.006	0.037±0.009	0.032±0.006
rDLPFC	0.088±0.021 (0.0000)	0.030±0.008	-	0.032±0.007	0.031±0.010	0.034±0.007 (0.0414)
rPPC	0.069±0.015 (0.0005)	0.033±0.007	0.029±0.007	-	0.032±0.008	0.015±0.004
VMPFC	0.033±0.006	0.036±0.007	0.030±0.006	0.022±0.004	-	0.029±0.008
PCC	0.029±0.004 (0.0029)	0.027±0.006	0.024±0.005	0.023±0.007	0.037±0.006	-

(A.2) Instantaneous influence F values (mean ± SE across subjects)

F(x.y)	rFIC	ACC	rDLPFC	rPPC	VMPFC	PCC
rFIC	-	0.354±0.047	0.125±0.031	0.121±0.028	0.126±0.029	0.132±0.037
ACC	x	-	0.298±0.064	0.193±0.044	0.072±0.016	0.207±0.049
rDLPFC	x	x	-	0.317±0.055	0.039±0.012	0.242±0.047
rPPC	x	x	x	-	0.027±0.009	0.144±0.032
VMPFC	x	x	x	x	-	0.107±0.021
PCC	x	x	x	x	x	

Table S4. (*Continued*).

(B) Visual oddball attention task

(B.1) Directed influence F values (mean ± SE across subjects)

F(x→y)	rFIC	ACC	rDLPFC	rPPC	VMPFC	PCC
rFIC	-	0.036±0.010	0.036±0.011	0.034±0.005	0.065±0.021	0.042±0.022
ACC	0.078±0.011 (0.0010)	-	0.022±0.004	0.028±0.009	0.035±0.008	0.033±0.007
rDLPFC	0.076±0.015 (0.0044)	0.045±0.014	-	0.049±0.012 (0.0303)	0.028±0.005	0.043±0.024
rPPC	0.058±0.015 (0.0286)	0.036±0.007 (0.0500)	0.024±0.005	-	0.039±0.009	0.022±0.006
VMPFC	0.042±0.009	0.034±0.010	0.034±0.011	0.036±0.010	-	0.051±0.021
PCC	0.033±0.010	0.030±0.009	0.023±0.005	0.032±0.006 (0.0052)	0.030±0.006	-

(B.2) Instantaneous influence F values (mean ± SE across subjects)

F(x.y)	rFIC	ACC	rDLPFC	rPPC	VMPFC	PCC
rFIC	-	0.420±0.069	0.176±0.027	0.232±0.037	0.101±0.065	0.126±0.038
ACC	x	-	0.241±0.053	0.264±0.052	0.057±0.020	0.211±0.047
rDLPFC	x	x	-	0.462±0.047	0.041±0.020	0.084±0.033
rPPC	x	x	x	-	0.050±0.014	0.156±0.057
VMPFC	x	x	x	x	-	0.082±0.022
PCC	x	x	x	x	x	-

Table S4. (*Continued*).

(C) Task-free resting state

(C.1) Directed influence F values (mean ± SE across subjects)

F(x→y)	rFIC	ACC	rDLPFC	rPPC	VMPFC	PCC
rFIC	-	0.049±0.008	0.036±0.008	0.031±0.005	0.044±0.008	0.042±0.009
ACC	0.110±0.014 (0.0000)	-	0.036±0.006	0.028±0.004	0.05±50.011	0.047±0.008
rDLPFC	0.069±0.007 (0.0000)	0.041±0.007	-	0.042±0.006	0.031±0.006	0.059±0.013
rPPC	0.063±0.009 (0.0001)	0.038±0.007	0.040±0.009	-	0.024±0.006	0.041±0.008
VMPFC	0.044±0.008	0.065±0.012	0.036±0.006	0.033±0.006 (0.0426)	-	0.065±0.013
PCC	0.079±0.013 (0.0013)	0.048±0.008	0.045±0.008	0.041±0.008	0.058±0.019	-

(C.2) Instantaneous influence F values (mean ± SE across subjects)

F(x.y)	rFIC	ACC	rDLPFC	rPPC	VMPFC	PCC
rFIC	-	0.253±0.034	0.127±0.021	0.080±0.017	0.088±0.018	0.081±0.019
ACC	x	-	0.193±0.027	0.117±0.019	0.100±0.017	0.236±0.045
rDLPFC	x	x	-	0.240±0.048	0.064±0.014	0.172±0.023
rPPC	x	x	x	-	0.030±0.007	0.099±0.025
VMPFC	x	x	x	x	-	0.140±0.027
PCC	x	x	x	x	x	-

(A.1, B.1, C.1) GCA directed influence terms $F_{x\to y}$ and $F_{y\to x}$ (mean ± SE, between pairs of regions across subjects). Influences are from column ROI to row ROI. Violet boxes indicate significant directed interactions, where the difference-of-influence term ($F_{x\to y}$ - $F_{y\to x}$) was significantly different from a bootstrap distribution at the group-level (Mann–Whitney U test, $P < 0.05$). The p-values (for significant $F_{x\to y}$ - $F_{y\to x}$) are reported within parenthesis inside the violet boxes; those p-values that survived an FDR correction ($q < 0.05$) for multiple comparisons are highlighted in blue (values indicated as 0.0000 refer to $P < 10^{-4}$).
(A.2, B.2, C.2) GCA instantaneous influence terms, $F_{x.y}$ (mean ± SE, between pairs of regions across subjects; the matrix is symmetric, so only upper triangular elements are shown). Red boxes indicate the optimal cluster configuration corresponding to a pairing of regions that maximizes sum of mutual instantaneous influences, $\Sigma F_{x.y}$. Across all tasks, the optimal pairs were identical with the SN (rFIC, ACC), CEN (rDLPFC, rPPC) and DMN (VMPFC, PPC).

Table S5. Network analysis of the causal interactions in the three experiments

ROI	Out-degree	In-degree	Out-In degree	Path length
		A. Auditory event segmentation		
rFIC	**3.00 ± 0.26**	**1.05 ± 0.18**	**+1.95 ± 0.38**	**1.22 ± 0.06**
ACC	1.15 ± 0.28	1.99 ± 0.30	−0.84 ± 0.53	1.44 ± 0.07
rDLPFC	1.06 ± 0.26	2.09 ± 0.24	−1.02 ± 0.46	1.41 ± 0.05
rPPC	1.24 ± 0.30	1.72 ± 0.31	−0.49 ± 0.55	1.47 ± 0.08
VMPFC	2.01 ± 0.33	1.52 ± 0.24	+0.49 ± 0.53	1.36 ± 0.07
PCC	1.57 ± 0.31	1.66 ± 0.31	−0.09 ± 0.53	1.49 ± 0.12
		B. Visual ″oddball″ attention		
rFIC	**1.86 ± 0.39**	**0.72 ± 0.24**	**+1.14 ± 0.54**	**1.61 ± 0.15**
ACC	0.94 ± 0.29	0.92 ± 0.29	+0.02 ± 0.49	1.87 ± 0.19
rDLPFC	0.49 ± 0.16	1.54 ± 0.34	−1.05 ± 0.36	1.68 ± 0.11
rPPC	0.87 ± 0.24	0.95 ± 0.23	−0.08 ± 0.35	2.06 ± 0.35
VMPFC	0.85 ± 0.29	0.87 ± 0.30	−0.02 ± 0.42	2.00 ± 0.24
PCC	0.67 ± 0.36	0.68 ± 0.23	−0.01 ± 0.47	1.93 ± 0.13
		C. Task-free resting state		
rFIC	**2.50 ± 0.25**	**0.81 ± 0.17**	**+1.70 ± 0.36**	**1.40 ± 0.07**
ACC	1.10 ± 0.23	1.53 ± 0.25	−0.43 ± 0.42	1.53 ± 0.05
rDLPFC	0.99 ± 0.28	1.56 ± 0.26	−0.57 ± 0.47	1.53 ± 0.07
rPPC	1.13 ± 0.25	1.24 ± 0.22	−0.11 ± 0.41	1.79 ± 0.24
VMPFC	1.05 ± 0.20	1.55 ± 0.21	−0.50 ± 0.33	1.62 ± 0.09
PCC	1.41 ± 0.31	1.49 ± 0.31	−0.08 ± 0.56	1.54 ± 0.12

Network analysis on the causal interactions identified with GCA revealed that the rFIC (boldface) had the highest out-degree, lowest in-degree, highest out-in degree, and shortest path length among all regions of the SN, CEN, and DMN. This indicates that the rFIC is a critical outflow hub at the intersection of the CEN and DMN.
Out-degree: Number of causal outflow connections from a node
In-degree: Number of causal in-flow connections to a node
Out-In-degree: Difference between ″Out-degree″ and ″In-degree″ (a measure of net causal outflow from a node)
Path length: Shortest path from a node to every other node in the network calculated by Dijkstra's algorithm (normalized by the number of nodes minus one).
Values of the metrics reported are mean ± SE across subjects.